Title: Localized electrical stimulation triggers cell-type-specific proliferation in biofilms

Authors: Colin J. Comerci¹†, Alan L. Gillman¹†, Leticia Galera-Laporta¹, Edgar Gutierrez², Alex Groisman², Joseph W. Larkin^{1#}, Jordi Garcia-Ojalvo³, Gürol M. Süel^{1,4}*

Affiliations:

¹Division of Biological Sciences, University of California San Diego, La Jolla, CA, USA 92093.

³Department of Experimental and Health Sciences, Universitat Pompeu Fabra, Barcelona, Spain 08003.

⁴San Diego Center for Systems Biology, University of California, San Diego, La Jolla, CA, USA 92093.

Present address: Departments of Biology and Physics, Boston University, Boston, MA, USA

*Corresponding Author: Gürol M. Süel, UC San Diego, Pacific Hall Room 2225B, Mail Code 0347, 9500 Gilman Dr, La Jolla, CA, USA 92093.

†These authors contributed equally to this manuscript.

Abstract: Biological systems ranging from bacteria to mammals utilize electrochemical signaling. While artificial electrochemical signals have been utilized to characterize neural tissue responses, the effects of such stimuli on non-neural systems remain unclear. To pursue this question, we developed an experimental platform that combines a microfluidic chip with a multi-electrode array (MiCMA) to enable localized electrochemical stimulation of bacterial biofilms. The device also allows simultaneous measurement of the physiological response within the biofilm with single-cell resolution. We find that stimulation of an electrode locally changes the ratio of the two major cell types comprising *Bacillus subtilis* biofilms, namely motile and extracellular matrix-producing cells. Specifically, stimulation promotes the proliferation of motile cells, but not matrix cells, even though these two cell types are genetically identical and reside in the same microenvironment. Our work thus reveals that an electronic interface can selectively target bacterial cell types, enabling control of biofilm composition and development.

Introduction

Since Wilhelm Roux's early experiments applying electric fields to developing eggs (Roux, 1892), the ability to electrically stimulate biological systems and monitor their response has formed a bedrock of bioelectrical research (Chang and Minc, 2014; Piccolino, 1997). Such exogenous stimulation provides a key avenue for understanding electrochemical effects in biological systems and developing novel applications and tools (Gokoffski et al., 2019; John et al., 2020; Liang et al., 2019; Zajdel et al., 2020). In particular, such technologies have been extensively utilized to study and understand electrically excitable cells such as neurons and cardiac cells (Cogan, 2008). More recent studies have revealed that electrochemical signaling via ions is not limited to such specialized cells, but rather represents a crucial form of communication across

²Department of Physics, University of California San Diego, La Jolla, CA, USA 92093.

diverse biological systems (Galera-Laporta et al., 2021; Prindle et al., 2015; Schofield et al., 2020). For example, such signaling appears to play key roles in the organization of multicellular organisms, including embryonic development, regeneration, and carcinogenesis (Levin, 2021; Levin et al., 2017; Yang and Brackenbury, 2013; Zhang et al., 2011), impacting fundamental cellular processes such as proliferation, differentiation, and migration (Blackiston et al., 2009; Funk, 2015; Humphries et al., 2017; Pai et al., 2015; Reid and Zhao, 2014; Strahl and Hamoen, 2010).

Various electrical stimulation techniques have been utilized in eukaryotic systems, leading to better understandings of action potentials in electrically excitable cells, embryogenesis, and wound healing (Chang and Minc, 2014; McCaig et al., 2005; Reid and Zhao, 2014). The application of electrical stimulation techniques to bacterial systems, such as biofilms, has also been explored, though these studies have been generally limited to: (1) the study of fast time-scale responses based on electron transfer and redox reactions (Bhokisham et al., 2020; Bird et al., 2019; El-Naggar et al., 2010; Lovley and Holmes, 2021; Terrell et al., 2021; Tschirhart et al., 2017). (2) electrically active species such as Shewanella (El-Naggar et al., 2010; Sydow et al., 2014), or genetically engineered strains (Bhokisham et al., 2020; Bird et al., 2019; Terrell et al., 2021; Tschirhart et al., 2017) used in microbial fuel cell research and bioelectrosynthesis (Dominika and Katarzyna, 2020; Lovley and Holmes, 2021), and (3) finally, most applications of electrical stimulation have focused on killing bacteria or disrupting biofilms for goals such as development of electroceuticals and wound healing (reviewed in Dominika and Katarzyna, 2020; Sultana et al., 2015). However, it remains unclear whether generic bacterial species that are not known to be electroactive, and especially those species that form biofilm communities, respond physiologically to a sub-lethal electrical stimulation (see perspective Jones and Larkin, 2021). In fact, a variety of recent works indicate that individual bacteria and biofilm communities use bioelectrical signaling for fundamental processes across a broad range of timescales such as mechanosensation (Bruni et al., 2017), antibiotic tolerance (Bruni et al., 2020; Lee et al., 2019), proliferation (Strahl and Hamoen, 2010; Stratford et al., 2019), inter-species attraction (Humphries et al., 2017), and coordination of metabolic activity (Liu et al., 2015; Prindle et al., 2015). There is thus a need to monitor fundamental physiological responses of bacteria, such as proliferation and cellular differentiation, in the context of electrical stimulation techniques.

In this study, we developed a device that integrates a microfluidic chip with a multielectrode array (MiCMA). This MiCMA device allowed us to expose a growing *Bacillus subtilis* biofilm to localized electrical stimuli and monitor a physiological response over many hours. We observed that stimulation exclusively triggers the proliferation of motile cells, which in turn locally alters the cell-type ratio of the biofilm. We also show that stimulated electrodes can locally increase the potassium ion concentration in the growth media, which alters the cell-type ratio in *Bacillus subtilis* biofilms. Together, these results suggest that electrochemical signals may play a role in regulating the cell-type composition of a biofilm community. The development of this MiCMA device and the demonstration of a cell-type-specific physiological response in biofilms sets the stage for novel approaches to control undomesticated bacteria and biofilms through electrical interfaces.

Results

In order to investigate whether electrical stimulation can trigger a response in bacterial communities, we developed an experimental platform that enables non-invasive local electrical stimulation in a developing biofilm, while simultaneously monitoring its effects with single-cell resolution. The device (Fig. 1A, B) is comprised of a polydimethylsiloxane (PDMS) microfluidic chip, which contains a biofilm growth chamber and medium perfusion channels (Fig. 1A, Fig. S1). This microfluidic chip is then attached to a transparent substrate containing a microelectrode array (MEA), which enables electrical stimulation of the biofilm (Fig. 1B). One of the important features of the device is its optical accessibility, which is facilitated by the small height (~5 µm) of the growth chamber. In addition, the chamber has horizontal dimensions of 2×2 mm², approximately matching the dimensions of the MEA (1.4×1.4 mm²), and can accommodate a biofilm with over a million cells (Fig. S2A). The MEA component contains 59 electrodes that are each 30 µm in diameter, spaced 200 µm apart, as well as a distant reference electrode (Fig. 1C, D). The large growth chamber allows ample space for biofilms to grow without quickly clogging the chamber, while the electrode array ensures that biofilms, which grow from random locations within the chamber (Fig. S2C vs. D), generally contain at least one electrode. Indeed, the array commonly allows multiple, independently controlled electrodes to become embedded within the same biofilm, which is ideal for control experiments. This device thus makes it possible to electrically stimulate small regions within a large biofilm during its development, and optically monitor cellular responses.

We first validated that biofilms can grow and develop within the assembled device. We measured the growth rate of *B. subtilis* biofilms in the MiCMA for over 12 hours by tracking the expansion of the biofilm edge using phase-contrast, time-lapse microscopy. We find that for a volumetric media flow rate of 50 μ L/h (corresponding to a flow speed of ~6 μ m/s in the growth chamber, Fig. S3), the average biofilm expansion rate is 14,460 ± 1,880 μ m²/hour (mean ± SEM, N = 16 biofilms, Fig. S2B). This biofilm growth rate is consistent with previous reports within microfluidic devices (Liu et al., 2015, 2017). Depending on the density of initially loaded cells, it took approximately 12-16 hours for biofilms to reach the size of hundreds of thousands of cells (radius > 250 μ m). These data demonstrate that large biofilms can be successfully grown and optically monitored for over 12 hours within our device.

Next, we evaluated the MiCMA's effect on local cation concentration. We focused on potassium, as it is the most abundant cation in any living cell, including bacterial cells. Importantly, potassium ions have previously been shown to be involved in cell-to-cell signaling and metabolic coordination within the biofilm (Liu et al., 2015; Prindle et al., 2015). We performed time-lapse imaging of the potassium sensitive fluorescent dye APG-4 in growth media supplemented with 300 mM KCl, near a stimulated electrode (Fig. 1E, Fig. S4A, and Movie S1). For electrical stimulation, we explored different protocols, took guidance from recent literature (Stratford et al., 2019, see Methods Section for more details) and opted to apply a monophasic pulsed signal with an amplitude of -3.0 V and a frequency of 50 Hz for 0.3 seconds (15 cycles of -3.0 V for 10 ms followed by 0 V for 10 ms). As anticipated, potassium becomes locally enriched near the stimulated electrode, with enrichment occurring within ~50 µm of the electrode edge and lasting for ~1 second (Fig. 1F, Fig. S4B, C). A similar potassium enrichment occurs near stimulated electrodes in the presence of cells, when the electrode is embedded within a biofilm (Fig. S4D, E).

Stimulation of an electrode within our device can thus locally and transiently enrich the concentration of potassium ions in the absence or presence of cells.

To determine whether electrochemical stimulation affects the biofilm, we decided to monitor the two main cell types that comprise B. subtilis biofilms, namely matrix-producing cells and motile cells (Kearns and Losick, 2005; López et al., 2010; Fig. 1F). Matrix-producing cells express components of the extracellular matrix, which forms a scaffold that holds the biofilm together and provides physical protection (Dufour et al., 2010; Govan and Deretic, 1996). Motile cells express components of the motility machinery, including flagella, and play an important role in biofilm initiation (Kazuo, 2007), dispersal (Ma et al., 2009), and competition with other bacterial species (Rosenberg et al., 2016). Within the biofilm, matrix-producing and motile cells co-exist, with motile cells held stationary in the densely packed community. It is commonly assumed that matrix cells promote biofilm stability, while motile cells may promote its dissociation. The ability to manipulate the cell-type ratio in a biofilm would thus provide a means to control its development. However, modulating the composition of cellular communities is a difficult task, since it would require selectively targeting specific cell types among genetically identical bacteria residing within the same microenvironment. We utilized MiCMA to investigate whether stimulation of an electrode that is embedded within the biofilm impacts the cell-type composition. In particular, we were interested in discerning among three alternative responses of the biofilm to local stimulation: (1) no change in the cell-type ratio, (2) an increase of matrix-producing cells near the electrode, or (3) an increase of motile cells near the electrode (Fig. 1H).

To optically monitor the cell type composition in *B. subtilis* biofilms, we constructed a transcriptional dual reporter strain that uniquely identifies matrix-producing and motile cell types based on their distinct promoter activities (Bai et al., 1993). Specifically, in motile cells the *hag* promoter expresses flagellar components (Mukherjee and Kearns, 2014), while in matrix-producing cells the *tasA* promoter expresses the amyloid fiber component of the extracellular matrix (Erskine et al., 2018). We integrated two single-copy transcriptional fluorescent reporter constructs, namely P_{hag} -YFP and P_{tasA} -mCherry, into the *B. subtilis* chromosome, and measured the activity of both promoters in the biofilm (Fig. 2A, B). Given that the two cell types are known to be mutually exclusive (Norman et al., 2013), we used the spectrally distinct fluorescence signals from each promoter-reporter to classify regions of the biofilm as either primarily motile (high P_{hag} -YFP signal and low P_{tasA} -mCherry signal) or matrix-producing (low P_{hag} -YFP signal and high P_{tasA} -mCherry signal) (Fig. 2C).

Motivated by the finding that electrical stimulation can locally increase potassium ion concentration (Fig. 1E above), we tested whether exposing a biofilm to an increased potassium concentration affects its cell-type ratio. For this purpose, we used a commercially available microfluidic device to grow biofilms and utilized automated control to transiently increase the potassium concentration in the growth media. Specifically, we periodically increased the potassium concentration in the growth media from the standard 8 mM to 300 mM KCl for 40 minutes every 4 hours. The duration of the elevated potassium exposures was chosen to ensure sufficient time for the high potassium media to fully penetrate the biofilm (Yang et al., 2020), while the extended interval between pulses was selected to provide sufficient time for the known membrane potential response dynamics of *B. subtilis* biofilms to subside (Prindle et al., 2015; see methods for details). Quantitative optical measurements of the biofilm area revealed that such

periodically increased potassium concentrations doubled the motile cell area from $30 \pm 5\%$ (mean \pm STD, Fig. 2D, E, Fig. S5A) to $64 \pm 5\%$ (mean \pm STD, Fig. 2F, G, Fig. S5B). We note that even a single exposure to elevated potassium concentration was able to increase motile cell area (Fig. S6A). However, consecutive exposures to transiently elevated potassium concentrations resulted in a greater effect (Fig. S6B), reversing the dominant cell type in the biofilm from matrix cells to motile cells. This data shows that changes in potassium concentration can lead to global changes in the cell-type composition of biofilms, suggesting that our electrical device may achieve a similar, but more spatially localized, response near a stimulated electrode.

To verify this expectation, we grew biofilms of the same double reporter strain in our MiCMA electrical device (Fig. 3A, B). Fluorescence time-lapse microscopy revealed that in contrast to unstimulated electrodes, which maintained relatively constant area fractions of motile and matrix cells over time (Figs. 3C, E, Figs. S7A, B and E, and Fig. S8A, Movie S2), the biofilm region surrounding the stimulated electrode (within 40 μ m) exhibits a clear increase in motile cell area over time (Figs. 3D, F, Figs. S7C, D, and E, and Fig. S8B, Movie S2). Specifically, 12 hours after stimulation, regions around the electrode had a motile cell area of 53 \pm 3% and a matrix area of 47 \pm 3%, while non-stimulated electrodes maintained a motile area of 30 \pm 9% (mean \pm STD, Fig. 3E, F). These data show that electrical stimulation causes a local increase in motile cells, similar to the global effect seen in biofilms exposed to higher potassium concentrations via media exchange (Fig. 2G above).

Given that changes to the extracellular potassium concentration (Prindle et al., 2015; Yang et al., 2020) as well as electrical stimulation (Stratford et al., 2019) can lead to changes in the membrane potential of *B. subtilis* cells, we also examined the electrochemical response of the cells surrounding stimulated electrodes. Specifically, we measured changes in the membrane potential of bacterial cells using the fluorescent dye Thioflavin-T (ThT), known to act as a Nernstian-potential reporter, such that a higher ThT fluorescent signal corresponds to a higher negative membrane potential (Prindle et al., 2015; Sahand et al., 2020; Stratford et al., 2019). By imaging ThT in biofilms formed by the dual reporter strain around stimulated electrodes, we found that the region enhanced in motile cells also has high ThT signal (Fig. S9A). In particular, while regions with low ThT signal consisted of $36 \pm 4\%$ motile cells, the high ThT regions around stimulated electrodes displayed $66 \pm 5\%$ motile cells (Fig. S9B). Thus, the local increase in motile cells correlates with cells that exhibit a more negative membrane potential.

The observed change in the cell-type composition in the MiCMA device upon electrode stimulation can be explained by two alternative scenarios (Fig. 3G): (1) there is an increased proliferation of motile cells near the stimulated electrode, or (2) matrix-producing cells switch to motile cells. To differentiate between these two scenarios, we turned to single-cell resolution imaging using confocal microscopy in the same device to study the electrode-biofilm interface. Using the dual reporter strain with spectrally distinct fluorescence reporters to identify cell types, we could classify individual cells as either motile or matrix cells (Fig. 4A-D, and S10). Compared to the unstimulated control electrode, we find that the number of motile cells increases near the stimulated electrodes (Figs. 4B, D, and Fig. S10). Specifically, we measured approximately 70,000 cells for each of six stimulated and six non-stimulated electrodes, and determined that the single-cell-level proportion of motile cells increases from approximately 30% around unstimulated electrodes (Fig. 4B) to over 50% in the vicinity of stimulated electrodes (Fig. 4D). The high 50%

local proportion of motile to matrix cells near the stimulated electrode gradually decreases to the basal value of 30% over a distance of approximately 15 µm from the edge of the electrode. These data show that the actual number of motile cells within the biofilm locally increases with closer proximity to stimulated electrodes. In addition to measuring the proportion of motile cells, we also determine the expression level of both promoters in individual cells. In particular, we quantified the ratio of *hag* (motile) to *tasA* (matrix) promoter activity for each cell surrounding stimulated and unstimulated electrodes (Fig. 4E). These data represent the induced functional state of each cell at the transcriptional level. We find that cells with closer proximity to the stimulated electrode exhibit higher *hag* to *tasA* promoter expression ratio (Fig. 4F), compared to the non-stimulated case (Fig. S11).

Finally, we tracked lineages of cells surrounding the stimulated electrode and, for each cell, we measured its *hag* and *tasA* promoter activities over 8 hours (Movie S3). Single-cell tracking did not reveal any cells that switched from motile to matrix-producing during our observation period. In fact, we find that cells typically maintain their promoter activities over time and throughout their lineage (Fig. 4G, H). Importantly, the data show that motile cells surrounding stimulated electrodes proliferate more than matrix-producing cells (Figs. 4G, H, and Fig. S12). The sub-second electrical stimulation thus locally and exclusively enhances motile cell proliferation near the electrode for several hours after stimulation (Fig. 4I).

Discussion

Externally applied electrical inputs have been successfully used to characterize the response of mammalian tissues, mainly of neural origin (Spira et al., 2019). Building on recent findings that electrical signals not only play a role in such specialized tissues, but also in bacteria and their biofilm communities (Bruni et al., 2017, 2020; Galera-Laporta et al., 2021; Lee et al., 2019; Prindle et al., 2015; Stratford et al., 2019), we set out to design a device (MiCMA) that allows local electrochemical stimulation of bacterial biofilms during growth. The MiCMA combines MEA technology with microfluidics, which allows single-cell monitoring of the biofilm in response to local electrical stimulation over several hours. As a proof of principle of this new technology, we focused here on how such stimulation may affect the different cell types of the biofilm community.

Our work reveals that *B. subtilis* biofilms respond to electrochemical stimulation in an unexpected way. Specifically, we find that while such stimulation alters a basic biological process, namely cellular proliferation, this response is cell-type specific. The connection between bioelectric signals and cell proliferation has been demonstrated, in both eukaryotic and prokaryotic systems (Blackiston et al., 2009; Levin et al., 2017; Strahl and Hamoen, 2010; Stratford et al., 2019). For example, in eukaryotes, potassium channels play a role in regulating stem cell proliferation (Peng et al., 2010). Similarly, proliferation of bacterial cells has been linked to electrical stimulation (Stratford et al., 2019), and the membrane potential is known to correlate with both cell elongation (Larkin et al., 2018; Lee et al., 2019) as well as division (Strahl and Hamoen, 2010). Here, we surprisingly find that in a biofilm, biochemical stimulation leads to the proliferation of a specific cell type (motile cells) (Fig. 4G and H). How this cell type-specific response is realized mechanistically is beyond the scope of this current work and remains to be

elucidated. It will be interesting to pursue and identify the molecular mechanisms that underlie electrochemically-mediated proliferation of a cell-type subset within a multicellular biofilm.

The use of artificial electrical stimulation has proven powerful in studying physiologically relevant bioelectrical signaling in eukaryotic systems (Chang and Minc, 2014; Reid and Zhao, 2014). Thus, the MiCMA device presented here may serve to probe and better understand bioelectrical signaling within bacterial biofilms. Interestingly, a recent study has shown that only a fraction of cells participates in such innate bioelectrical signaling within *B. subtilis* biofilms (Larkin et al., 2018). The cell-type specific response to exogenous electrical stimulation reported here may thus be related to the heterogeneity of biofilm action potentials. It is also possible that the innate action potentials in *B. subtilis* biofilms could play a role in regulating the cell-type composition during biofilm development.

Results from *Planaria* and frog embryos show that bioelectrical signaling plays an important role in organ development, and that exogenous electrical stimulation can lead to the growth of ectopic organs (Levin et al., 2017; Oviedo et al., 2010; Pai et al., 2012). These processes are driven by the proliferation of specific cell types. Our demonstration of cell-type specific proliferation in bacterial biofilms triggered by an electrochemical stimulation establishes a prokaryotic paradigm to study the effects of electrochemical signals during biological self-organization and development. Given the experimental accessibility of bacteria in terms of ease of manipulation and observation, perhaps such a prokaryotic model system would provide the opportunity to possibly identify shared conceptual principles underlying multicellular community organization during development.

From a more applied perspective, our results illustrate the possibility of using electrical-based approaches for biofilm control. Increasing the number of motile cells concurrently reduces the fraction of cells that synthesize the extracellular matrix. Since the extracellular matrix provides physical protection and holds the biofilm together (Dufour et al., 2010; Govan and Deretic, 1996), a reduction in the percentage of matrix cells could weaken the physical integrity of the biofilm, possibly leading to the dispersal of the community. Since the extracellular matrix also provides a physical barrier that hinders chemicals from diffusing into the biofilm (Jefferson et al., 2005; Singh et al., 2010; Tseng et al., 2013), reducing the matrix cell fraction could enhance the access of antibiotics to the biofilm. Consequently, it may be possible to develop future electrical-based approaches to control and manipulate the development and life cycle of biofilm communities that are pervasive throughout our environment. Such advances may also be of interest to other fields such as synthetic biology to engineer bacterial communities with desired physical and biological properties.

References

- Bai, U., Mandic-Mulec, I., and Smith, I. (1993). SinI modulates the activity of SinR, a developmental switch protein of Bacillus subtilis, by protein-protein interaction. Gene Dev 7, 139–148.
- Bhokisham, N., VanArsdale, E., Stephens, K.T., Hauk, P., Payne, G.F., and Bentley, W.E. (2020). A redox-based electrogenetic CRISPR system to connect with and control biological information networks. Nat Commun 11, 2427.
- Bird, L.J., Onderko, E.L., Phillips, D.A., Mickol, R.L., Malanoski, A.P., Yates, M.D., Eddie, B.J., and Glaven, S.M. (2019). Engineered living conductive biofilms as functional materials. Mrs Commun *9*, 505–517.
- Blackiston, D.J., McLaughlin, K.A., and Levin, M. (2009). Bioelectric controls of cell proliferation: ion channels, membrane voltage and the cell cycle. Cell Cycle 8, 3527–3536.
- Bruni, G.N., Weekley, R.A., Dodd, B.J.T., and Kralj, J.M. (2017). Voltage-gated calcium flux mediates Escherichia coli mechanosensation. Proc National Acad Sci 201703084.
- Bruni, G.N., Kralj, J.M., Garrett, W.S., Laub, M.T., Ezraty, B., and Lee, D. (2020). Membrane voltage dysregulation driven by metabolic dysfunction underlies bactericidal activity of aminoglycosides. Elife 9, e58706.
- Chang, F., and Minc, N. (2014). Electrochemical Control of Cell and Tissue Polarity. Annu Rev Cell Dev Bi 30, 317–336.
- Cogan, S.F. (2008). Neural Stimulation and Recording Electrodes. Annu Rev Biomed Eng 10, 275–309.
- Dominika, C.-G., and Katarzyna, K. (2020). A journey in the complex interactions between electrochemistry and bacteriology: From electroactivity to electromodulation of bacterial biofilms. Bioelectrochemistry *131*, 107401.
- Dufour, D., Leung, V., and Lévesque, C.M. (2010). Bacterial biofilm: structure, function, and antimicrobial resistance. Endodontic Topics 22, 2–16.
- El-Naggar, M.Y., Wanger, G., Leung, K.M., Yuzvinsky, T.D., Southam, G., Yang, J., Lau, W.M., Nealson, K.H., and Gorby, Y.A. (2010). Electrical transport along bacterial nanowires from *Shewanella oneidensis* MR-1. Proc National Acad Sci *107*, 18127.
- Erskine, E., MacPhee, C.E., and Stanley-Wall, N.R. (2018). Functional Amyloid and Other Protein Fibers in the Biofilm Matrix. Journal of Molecular Biology *430*, 3642–3656.
- Funk, R.H.W. (2015). Endogenous electric fields as guiding cue for cell migration. Front Physiol 6, 143–143.
- Galera-Laporta, L., Comerci, C.J., Garcia-Ojalvo, J., and Süel, G.M. (2021). IonoBiology: The functional dynamics of the intracellular metallome, with lessons from bacteria. Cell Systems *12*, 497–508.
- Gokoffski, K.K., Jia, X., Shvarts, D., Xia, G., and Zhao, M. (2019). Physiologic Electrical Fields Direct Retinal Ganglion Cell Axon Growth In Vitro. Invest Ophth Vis Sci 60, 3659–3668.
- Govan, J.R., and Deretic, V. (1996). Microbial pathogenesis in cystic fibrosis: mucoid Pseudomonas aeruginosa and Burkholderia cepacia. Microbiol Rev 60, 539–574.
- Humphries, J., Xiong, L., Liu, J., Prindle, A., Yuan, F., Arjes, H.A., Tsimring, L., and Süel, G.M. (2017). Species-Independent Attraction to Biofilms through Electrical Signaling. Cell *168*, 200-209.e12.

- Jefferson, K.K., Goldmann, D.A., and Pier, G.B. (2005). Use of confocal microscopy to analyze the rate of vancomycin penetration through Staphylococcus aureus biofilms. Antimicrob Agents Ch *49*, 2467–2473.
- John, S., Mohammad, J., Juanita, M., Manping, J., Pattawong, P., Harika, D., Chunxiao, W., Sergio, C., Alexander, F., Nebyu, Y., et al. (2020). Machine Learning-Driven Bioelectronics for Closed-Loop Control of Cells. Adv Intelligent Syst *2*, 2000140.
- Jones, J.M., and Larkin, J.W. (2021). Toward Bacterial Bioelectric Signal Transduction. Bioelectr 3, 116–119.
- Kazuo, K. (2007). Bacillus subtilis Pellicle Formation Proceeds through Genetically Defined Morphological Changes. J Bacteriol *189*, 4920–4931.
- Kearns, D.B., and Losick, R. (2005). Cell population heterogeneity during growth of Bacillus subtilis. Gene Dev 19, 3083–3094.
- Larkin, J.W., Zhai, X., Kikuchi, K., Redford, S.E., Prindle, A., Liu, J., Greenfield, S., Walczak, A.M., Garcia-Ojalvo, J., Mugler, A., et al. (2018). Signal Percolation within a Bacterial Community. Cell Syst 7, 137-145.e3.
- Lee, D.-Y.D., Galera-Laporta, L., Bialecka-Fornal, M., Moon, E.C., Shen, Z., Briggs, S.P., Garcia-Ojalvo, J., and Süel, G.M. (2019). Magnesium Flux Modulates Ribosomes to Increase Bacterial Survival. Cell *177*, 352-360.e13.
- Levin, M. (2021). Bioelectric signaling: Reprogrammable circuits underlying embryogenesis, regeneration, and cancer. Cell *184*, 1971–1989.
- Levin, M., Pezzulo, G., and Finkelstein, J.M. (2017). Endogenous Bioelectric Signaling Networks: Exploiting Voltage Gradients for Control of Growth and Form. Annu Rev Biomed Eng 19, 353–387.
- Liang, G., Houpu, L., Yuan, W., Zhuo, L., John, A., Min, Z., and Quan, Q. (2019). Controlling ERK Activation Dynamics in Mammary Epithelial Cells with Alternating Electric Fields through Microelectrodes. Nano Lett *19*, 7526–7533.
- Liu, J., Prindle, A., Humphries, J., Gabalda-Sagarra, M., Asally, M., Lee, D.D., Ly, S., Garcia-Ojalvo, J., and Süel, G.M. (2015). Metabolic co-dependence gives rise to collective oscillations within biofilms. Nature *523*, 550–554.
- Liu, J., Martinez-Corral, R., Prindle, A., Lee, D.D., Larkin, J., Gabalda-Sagarra, M., Garcia-Ojalvo, J., and Süel, G.M. (2017). Coupling between distant biofilms and emergence of nutrient time-sharing. Science *356*, 638.
- López, D., Vlamakis, H., and Kolter, R. (2010). Biofilms. Csh Perspect Biol 2.
- Lovley, D.R., and Holmes, D.E. (2021). Electromicrobiology: the ecophysiology of phylogenetically diverse electroactive microorganisms. Nat Rev Microbiol 1–15.
- Ma, L., Conover, M., Lu, H., Parsek, M.R., Bayles, K., and Wozniak, D.J. (2009). Assembly and development of the Pseudomonas aeruginosa biofilm matrix. Plos Pathog *5*, e1000354–e1000354.
- McCaig, C.D., Rajnicek, A.M., Bing, S., and Zhao, M. (2005). Controlling Cell Behavior Electrically: Current Views and Future Potential. Physiol Rev 85, 943–978.
- Mukherjee, S., and Kearns, D.B. (2014). The Structure and Regulation of Flagella in Bacillus subtilis. Annu Rev Genet 48, 319–340.
- Norman, T.M., Lord, N.D., Paulsson, J., and Losick, R. (2013). Memory and modularity in cell-fate decision making. Nature *503*, 481–486.

- Oviedo, N.J., Morokuma, J., Walentek, P., Kema, I.P., Gu, M.B., Ahn, J.-M., Hwang, J.S., Gojobori, T., and Levin, M. (2010). Long-range neural and gap junction protein-mediated cues control polarity during planarian regeneration. Dev Biol *339*, 188–199.
- Pai, V.P., Aw, S., Shomrat, T., Lemire, J.M., and Levin, M. (2012). Transmembrane voltage potential controls embryonic eye patterning in Xenopus laevis. Development *139*, 313–323.
- Pai, V.P., Martyniuk, C.J., Echeverri, K., Sundelacruz, S., Kaplan, D.L., and Levin, M. (2015). Genome-wide analysis reveals conserved transcriptional responses downstream of resting potential change in Xenopus embryos, axolotl regeneration, and human mesenchymal cell differentiation. Regen *3*, 3–25.
- Peng, J., N., R., Stephanie, Chi-wing, K., Jidong, F., Kuo-Ti, L., Deborah, W., C., Camie, Wenbin, D., and A., L., Ronald (2010). Electrophysiological properties of human induced pluripotent stem cells. Am J Physiol-Cell Ph *298*, C486–C495.
- Piccolino, M. (1997). Luigi Galvani and animal electricity: two centuries after the foundation of electrophysiology. Trends in Neurosciences 20, 443–448.
- Prindle, A., Liu, J., Asally, M., Ly, S., Garcia-Ojalvo, J., and Süel, G.M. (2015). Ion channels enable electrical communication in bacterial communities. Nature *527*, 59–63.
- Reid, B., and Zhao, M. (2014). The Electrical Response to Injury: Molecular Mechanisms and Wound Healing. Adv Wound Care 3, 184–201.
- Rosenberg, G., Steinberg, N., Oppenheimer-Shaanan, Y., Olender, T., Doron, S., Ben-Ari, J., Sirota-Madi, A., Bloom-Ackermann, Z., and Kolodkin-Gal, I. (2016). Not so simple, not so subtle: the interspecies competition between Bacillus simplex and Bacillus subtilis and its impact on the evolution of biofilms. Npj Biofilms Microbiomes 2, 15027.
- Roux, W. (1892). Über die morphologische Polarisation von Eiern und Embryonen durch den electrischen Strom. Sitzungsber. Acad. Wiss. Wien Math. Naturwiss. 1, 27–228.
- Sahand, P., S., C., Marko, and Y., E.-N., Mohamed (2020). Spatiotemporal mapping of bacterial membrane potential responses to extracellular electron transfer. Proc National Acad Sci 117, 20171.
- Schofield, Z., Meloni, G.N., Tran, P., Zerfass, C., Sena, G., Hayashi, Y., Grant, M., Contera, S.A., Minteer, S.D., Kim, M., et al. (2020). Bioelectrical understanding and engineering of cell biology. J Roy Soc Interface *17*, 20200013.
- Singh, R., Ray, P., Das, A., and Sharma, M. (2010). Penetration of antibiotics through Staphylococcus aureus and Staphylococcus epidermidis biofilms. J Antimicrob Chemoth 65, 1955–1958.
- Spira, M.E., Huang, S.-H., Shmoel, N., and Erez, H. (2019). Multisite Intracellular Recordings by MEA. ["Michela Chiappalone", "Valentina Pasquale", and "Monica Frega"], eds. (Cham: Springer International Publishing), pp. 125–153.
- Strahl, H., and Hamoen, L.W. (2010). Membrane potential is important for bacterial cell division. Proc National Acad Sci *107*, 12281--12286.
- Stratford, J.P., Edwards, C.L.A., Ghanshyam, M.J., Malyshev, D., Delise, M.A., Hayashi, Y., and Asally, M. (2019). Electrically induced bacterial membrane-potential dynamics correspond to cellular proliferation capacity. Proc National Acad Sci *116*, 9552--9557.
- Sultana, S.T., Babauta, J.T., and Beyenal, H. (2015). Electrochemical biofilm control: a review. Biofouling *31*, 745–758.
- Sydow, A., Krieg, T., Mayer, F., Schrader, J., and Holtmann, D. (2014). Electroactive bacteria—molecular mechanisms and genetic tools. Appl Microbiol Biot *98*, 8481–8495.

- Terrell, J.L., Tschirhart, T., Jahnke, J.P., Stephens, K., Liu, Y., Dong, H., Hurley, M.M., Pozo, M., McKay, R., Tsao, C.Y., et al. (2021). Bioelectronic control of a microbial community using surface-assembled electrogenetic cells to route signals. Nat Nanotechnol *16*, 688–697.
- Tschirhart, T., Kim, E., McKay, R., Ueda, H., Wu, H.-C., Pottash, A.E., Zargar, A., Negrete, A., Shiloach, J., Payne, G.F., et al. (2017). Electronic control of gene expression and cell behaviour in Escherichia coli through redox signalling. Nat Commun *8*, 14030.
- Tseng, B.S., Zhang, W., Harrison, J.J., Quach, T.P., Song, J.L., Penterman, J., Singh, P.K., Chopp, D.L., Packman, A.I., and Parsek, M.R. (2013). The extracellular matrix protects Pseudomonas aeruginosa biofilms by limiting the penetration of tobramycin. Environ Microbiol 15, 2865–2878.
- Yang, M., and Brackenbury, W.J. (2013). Membrane potential and cancer progression. Front Physiol 4, 185–185.
- Yang, C.-Y., Bialecka-Fornal, M., Weatherwax, C., Larkin, J.W., Prindle, A., Liu, J., Garcia-Ojalvo, J., and Süel, G.M. (2020). Encoding Membrane-Potential-Based Memory within a Microbial Community. Cell Syst *10*, 417-423.e3.
- Zajdel, T.J., Shim, G., Wang, L., Rossello-Martinez, A., and Cohen, D.J. (2020). SCHEEPDOG: Programming Electric Cues to Dynamically Herd Large-Scale Cell Migration. Cell Syst 10, 506-514.e3.
- Zhang, D., Chan, J.D., Nogi, T., and Marchant, J.S. (2011). Opposing Roles of Voltage-Gated Ca2+ Channels in Neuronal Control of Regenerative Patterning. J Neurosci *31*, 15983.

Fig. 1. A novel experimental platform for localized electrical stimulation of biofilms. (A) Left: schematic of the two-layer PDMS microfluidic chip developed for this study. Right: photograph of the microfluidic device. Engraved on the bottom surface of the chip are a perfusion flow channels with one media outlet and one or more inlets and a 2 mm x 2 mm square biofilm growth chamber. Embedded in the chip are air channels, which expose the top of the 100 µm-thick PDMS roof of the growth chamber to atmospheric air, facilitating aerobic growth of bacteria in the chamber (Fig. S1). (B) Left: schematic of the MEA substrate with 60 electrodes embedded in the glass carrier material—59 for the electrode array and one reference electrode. Microelectrodes connect to the control headstage by corresponding electrode tracks and contact pads on the periphery. Right: photograph of the MEA. To better visualize MEA components, we show an MEA with electrodes and tracks made of gold. For experiments, titanium nitride electrodes and transparent indium tin oxide tracks were used. The PDMS chip is reversibly attached to the MEA by applying vacuum suction to an O-shaped vacuum cup on the chip to form the assembled MiCMA device. (C) Phase-contrast image of the MEA in the assembled device. PDMS pillars provide structural support for the ~5 μm-deep growth chamber (scale bar 200 μm). (**D**) Close-up image of an electrode (scale bar 20 µm). (E) Filmstrip of the fluorescent potassium reporter dye APG-4 near an electrode (white circle) before and after stimulation (stimulation shown in yellow, at 0 seconds). The fluorescence intensity indicates the relative potassium concentration (scale bar 50 μm). (F) Radial average of the relative potassium concentration as a function of distance to the edge of the electrode. The plots are shown for each timepoint in (E). (G) Cartoon depiction of a bacterial biofilm comprised of two cell types: motile cells (green) and extracellular matrixproducing cells (magenta). Throughout the figures, motile cells will be shown in green and matrixproducing cells in magenta. Electrical stimulation is applied to an electrode embedded within the biofilm (yellow and black circle). (H) Electrical stimulation of a biofilm could produce one of three possible responses: 1) no change to the ratio of motile and matrix-producing cells, 2) a local increase in matrix-producing cells, or 3) a local increase in motile cells.

Fig. 2. Transient enrichment of potassium in the growth media increases the percentage of motile cells within the biofilm. (A) Schematic of the *Bacillus subtilis* transcriptional dual-reporter strain. Motile cells express YFP under the control of the *hag* promoter while matrix-producing cells express mCherry under the control of the *tasA* promoter. (B) Phase-contrast (left) and fluorescence images (right) of the bottom right quarter of a biofilm grown in conventional media (t = 15 hr). (C) A pixel classification algorithm (Supplementary Text) is used to identify each pixel as either primarily matrix-producing or motile, creating a pixel map of the image from (B). (D) Filmstrip of cell type pixel maps for a biofilm growing in standard MSgg growth medium. (E) Plot of the average motile and matrix area percent for biofilms grown in standard growth media (8 mM KCl) as a function of time. (F) Filmstrip of cell type pixel maps for a biofilm that is periodically shocked with growth media supplemented with 300 mM KCl for 40 minutes every 4 hours. (G) Plot of the average motile and matrix area percent for biofilms shocked with KCl. The light-orange bars represent periods where media was supplemented with 300 mM KCl using a microfluidic system. In (E) and (G), N = 8 biofilms; error bars are mean \pm STD. (Scale bars 100 μ m)

Fig. 3. Electrical stimulation leads to a localized increase in the percentage of motile cells. (A) Phase-contrast and (B) fluorescence microscopy images of a *B. subtilis* biofilm grown in the MiCMA, prior to electrical stimulation (scale bar 200 μm). (C) Filmstrip of fluorescence microscopy images around an non-stimulated electrode. (D) Filmstrip of fluorescence microscopy images following -3.0 V electrical stimulation. The area of motile cells increases locally around

the electrode (scale bar 20 μ m). (E) Plot of the cell-type area percent in the 40 μ m region around non-stimulated electrodes as a function of time (N = 4 electrodes; mean \pm STD). (F) Plot of the cell-type area percent in the 40 μ m region around stimulated electrodes as a function of time (N = 8 electrodes; mean \pm STD). (G) Cartoon depiction of the two alternative scenarios that would lead to a local change in the cell-type ratio: 1) increased proliferation of motile cells relative to matrix-producing cells; 2) matrix-producing cells switch gene expression to become motile cells.

Fig. 4. Electrical stimulation causes a local increase in motile-cell type proliferation. (A) Confocal fluorescence image showing single motile (green) and matrix-producing (magenta) cells surrounding a non-stimulated electrode. Image acquired 12 hours after stimulation of an adjacent electrode (scale bar 10 µm). (B) Average local percent of motile and matrix cells as a function of distance from the edge of the electrode for non-stimulated electrodes 12 hours after stimulation of an adjacent electrode (N = 6 electrodes from 3 independent experiments mean \pm SEM). (C) Confocal fluorescence image around a stimulated electrode. Image acquired 12 hours after stimulation. (D) Average local cell type percent as a function of distance from the edge of the electrode 12 hours after stimulation (N = 6 electrodes, mean \pm SEM). (E) Confocal image for the stimulated electrode from (C), pseudo-colored by the natural log of the ratio of motile/matrix gene expression for each cell. (F) Mean single-cell gene expression ratio as a function of distance from the electrode (N = 6, mean \pm SEM). (G, H) Representative lineage tree from a single initial motile (G) and matrix-producing (H) progenitor cell at the electrode edge. The branches of the tree are colored according to the measured single-cell gene expression ratio as a function of time. (I) Cartoon depiction of the localized, cell-type-specific response of a biofilm (left) to electrical stimulation. Stimulation of an embedded electrode (yellow circle) causes enhanced proliferation of motile cells, near the stimulated electrode (right).

Figure 1

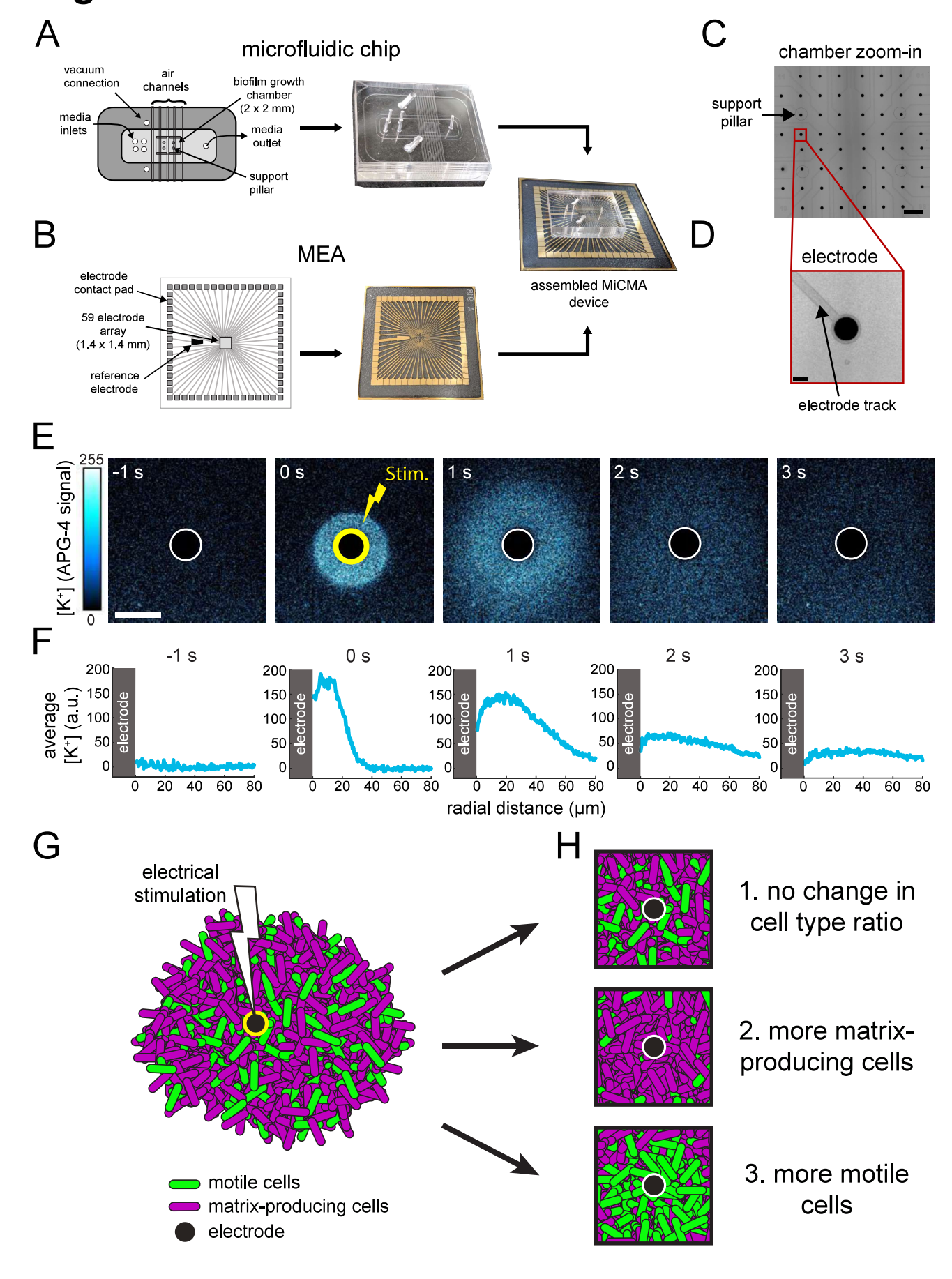


Figure 2 A

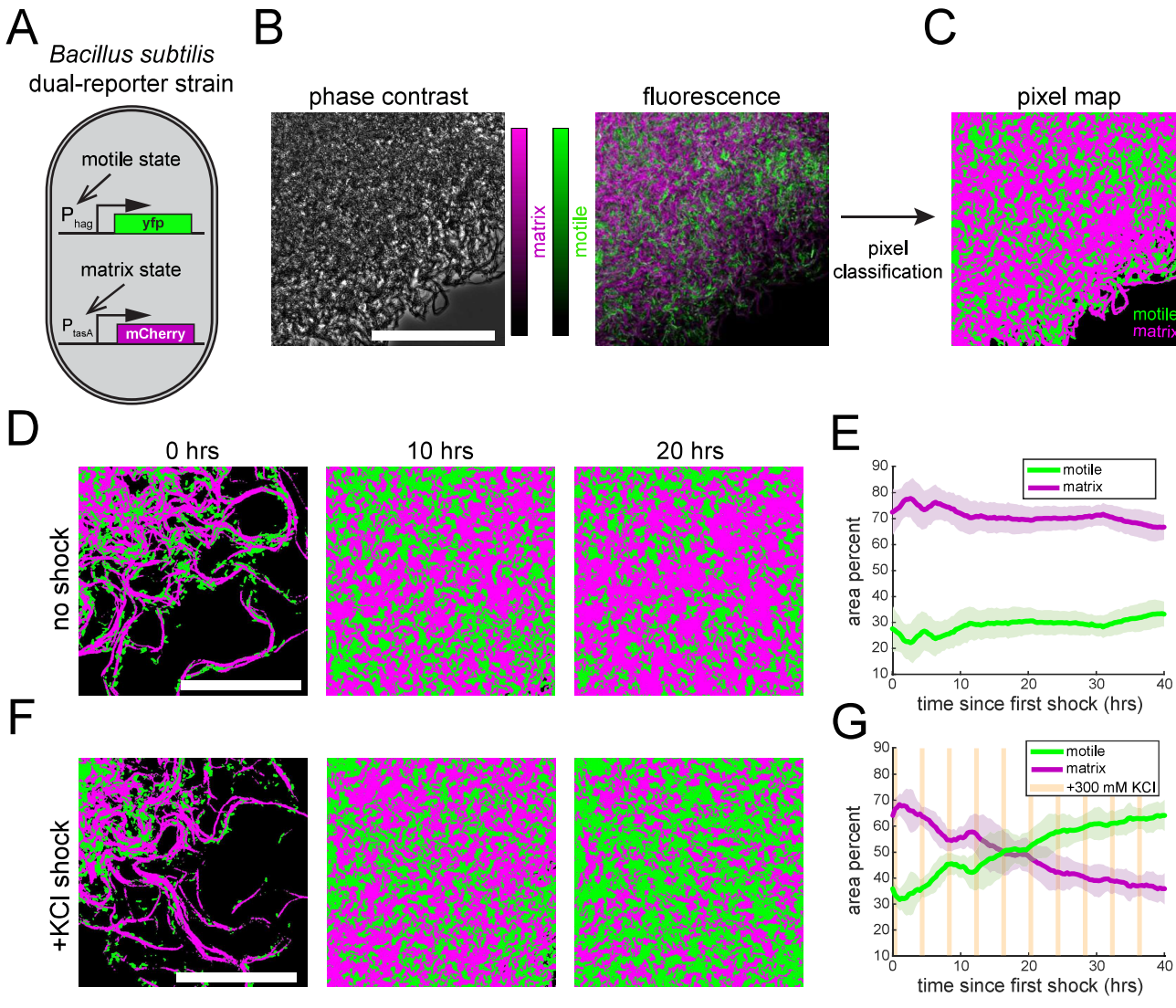


Figure 3

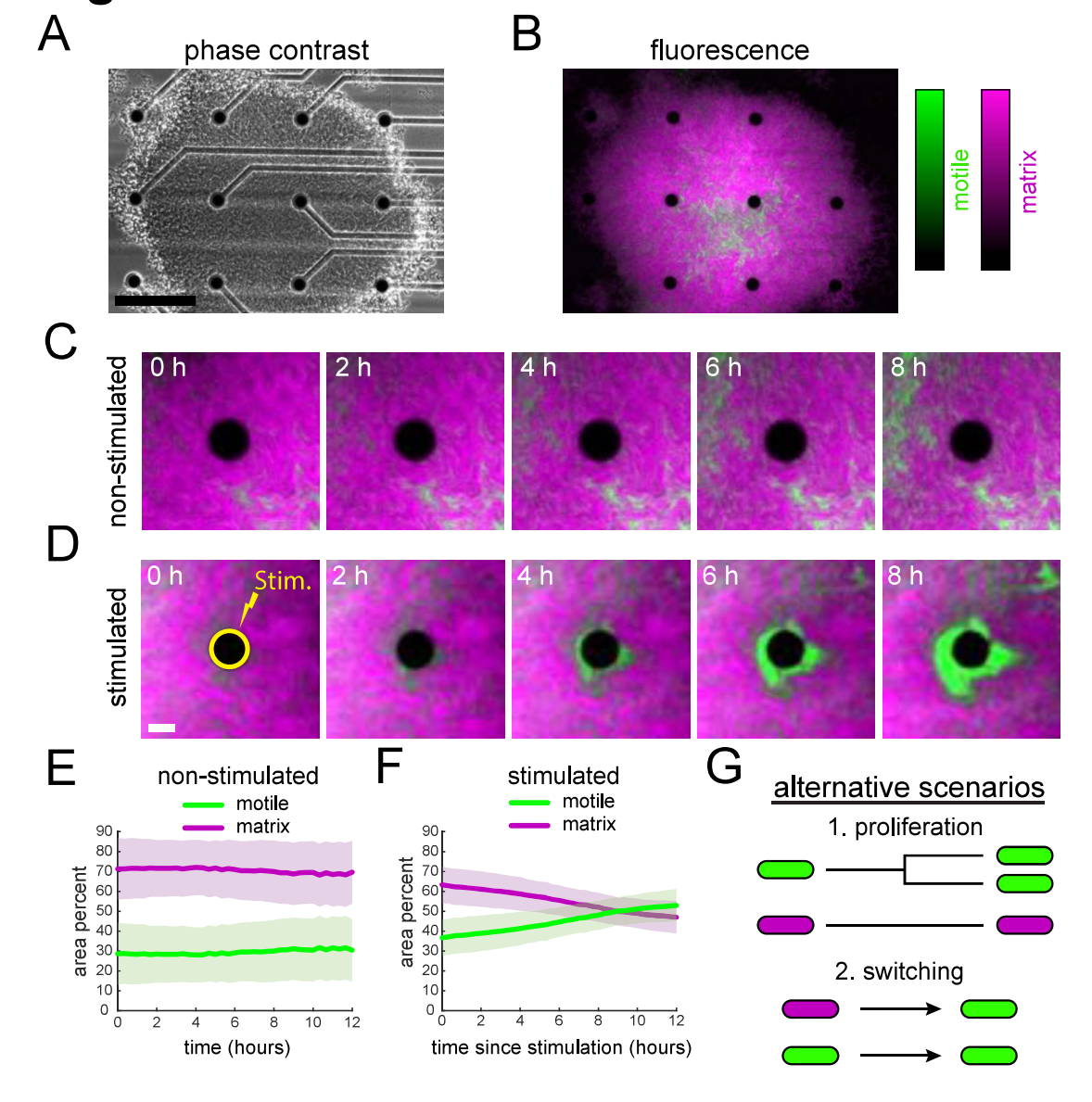
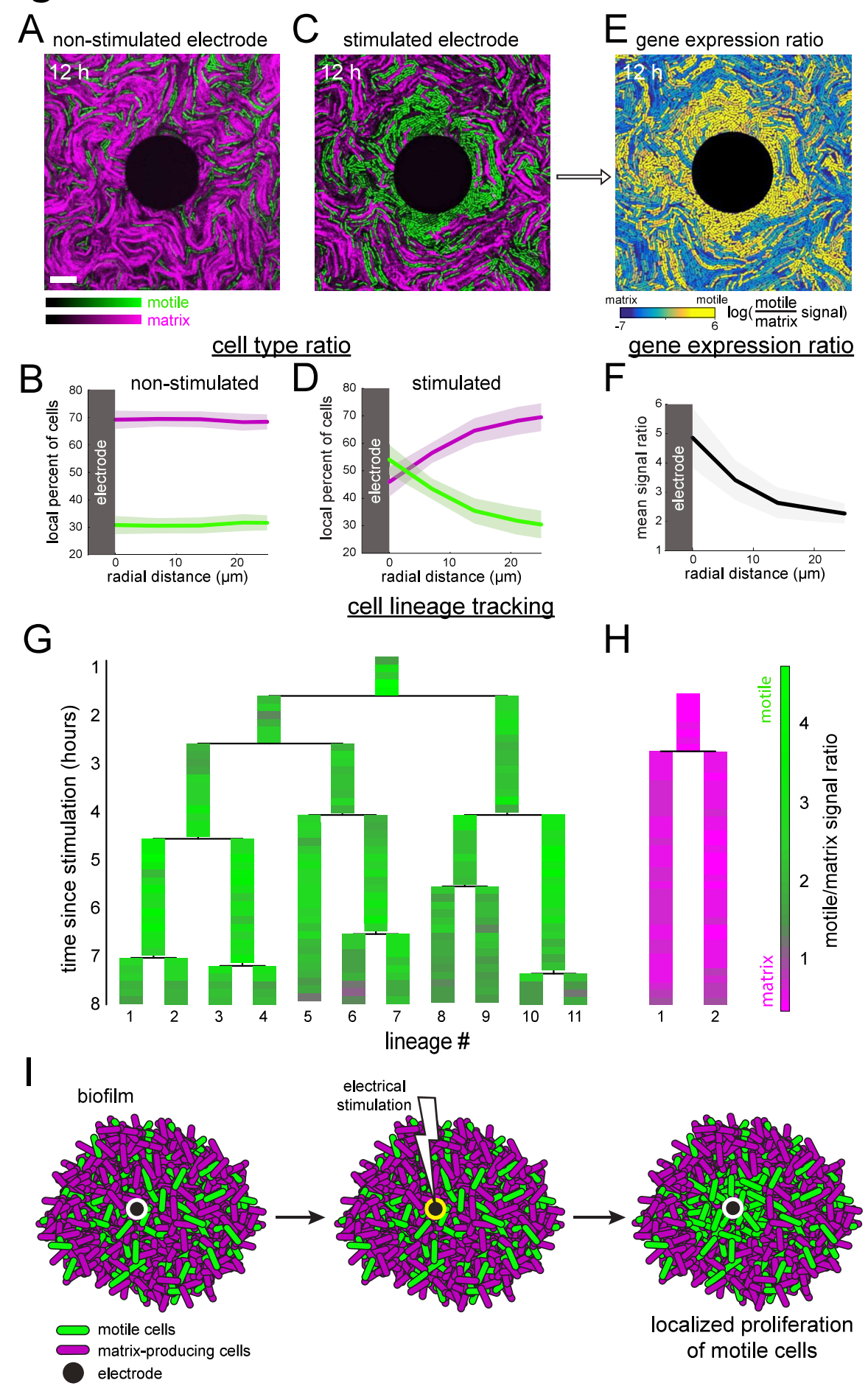


Fig. 4



Materials and Methods

Bacillus subtilis strains

We conducted all experiments with *Bacillus subtilis* NCIB 3610 *amyE::Phag-yfp* (Spec^R) *sacA::PtasA-tsr-mcherry* (Cm^R). Wild-type 3610 was a gift from W. Winkler (Irnov and Winkler, 2010).

Microfluidic device

The microfluidic device is formed by sealing a polydimethylsiloxane (PDMS) microfluidic chip against the microelectrode array (MEA, discussed below). The microfluidic chip is made out of two layers of silicone, 0.5 and 4 mm-thick, which are bonded together using oxygen plasma treatment. The 0.5 mm thick layer is proximal to the substrate and has microchannels of three different depths, 15, 25, and 45 µm, which are engraved on the side facing the substrate and form a network of microchannels with a shallow biofilm growth chamber and deep medium supply (perfusion) channels (Fig S1). In addition, a wide O-shaped, 45 µm-deep groove surrounding the network of liquid-filled channels serves as a vacuum cup to seal the chip against the substrate (Fig. S1). The master mold to cast the 0.5 mm thick-layer is a silicon wafer with a three-level micro-relief, which is created using UV-photolithography in a three-step process with a SU8 UV-curable epoxy (SU8-2015) as described elsewhere (VanDelinder and Groisman, 2007). The second, 4 mm-thick layer of the chip has an array of 75 µm deep, 250 µm wide channels engraved on its side facing the 0.5 mm layer. The master mold for this second layer is another silicon wafer with a 75 µm-tall relief, which is also created using UV-photolithography with a SU8 photoresist (SU8-2050). Both layers of the chip are made out of Sylgard 184 polydimethylsiloxane (Dow Corning; base and curing agent mixed at 10:1).

In a finished microfluidic chip, the 75 µm-deep and 250 µm-wide channels are embedded at a distance of 0.5 mm from the side facing the substrate and are open to the atmosphere at the edges of the chip, which are perpendicular to the channels. Because the oxygen permeability of air is $\sim 10^5$ times greater than that of PDMS, the oxygen content of air everywhere in the embedded channels thus corresponds to its atmospheric levels. The barrier of the oxygen supply to the biofilm growth chamber in the central area of the microfluidic device is due to the 0.5 mm layer of PDMS between the growth chamber and the embedded channels, making the oxygen supply to the biofilm ~ 10 times more efficient than in a typical 5 mm-thick microfluidic device.

Microelectrode array

Commercially available 60ThinMEA200/30iR-ITO-w/o (Multi Channel Systems GmbH) MEAs were used for all experiments. This MEA has a 180 µm-thin recording field to allow for high NA immersion microscopy. Embedded in the glass carrier material are 59 titanium nitride (TiN) stimulation electrodes and one internal reference electrode (Fig. 1B). Electrodes are 30 µm in diameter and are arranged in an 8x8 grid with 200 µm electrode spacing. Silicon nitride (SiN) is used as an electrical isolating layer. Transparent indium tin oxide (ITO) conductive strips form the tracks that connect the electrode to its corresponding contact pad for integration and control by the MEA-2100-2x60 headstage. Prior to use, the microelectrode array was cleaned and sterilized according to the manufacturer's recommended protocol. Briefly, the substrate was soaked in a detergent solution overnight with agitation, rinsed thoroughly with distilled water,

and autoclaved at 121°C for 30 min. Sterilized MEAs were stored in sterile distilled water at 4°C in the dark to maintain a hydrophilic surface.

MiCMA device assembly

The microfluidic chip is sealed to the sterilized microelectrode array substrate to form the completed device (MiCMA) by applying vacuum at a gauge pressure of -21 kPa to the O-shaped groove around the microchannel network. The application of vacuum causes partial collapse of the microchannels in the network. The collapse is more pronounced for wider microchannels and in central areas of microchannels. In particular, the supporting pillars in the central area of the 4 mm-wide perfusion channel (four circles and four rectangles with rounded corners), which are 15 um above the substrate without vacuum, collapse all the way to the substrate and become compressed under the vacuum. The $\sim 2x^2$ mm² central area, which is originally 25 µm above the substrate, collapses under the vacuum to ~5 µm, forming a shallow chamber, where the biofilm grows. Once the supporting pillars touch the substrate, the collapse of the central area under vacuum is substantially slowed down, making it possible to precisely control the depth of the growth chamber and maintain a uniform depth. The device was filled with medium and inoculated with bacterial suspension (see below). The inlet and outlet ports of the device were connected to medium reservoirs, and the device was perfused at a constant rate. The assembled device was placed into an MES-2100-2x60 headstage (Multi Channel Systems GmbH) for stimulation after growth.

Biofilm growth conditions

For all experiments, we grew biofilms in MSgg medium containing 5 mM potassium phosphate buffer (pH 7.0), 100 mM MOPS buffer (pH 7.0, adjusted using NaOH), 2 mM MgCl₂, 700 μ M CaCl₂, 50 μ M MnCl₂, 100 μ M FeCl₃, 1 μ M ZnCl₂, 2 μ M thiamine HCl, 0.1 mM sodium citrate, 0.5% (v/v) glycerol and 0.4% (w/v) monosodium glutamate. Media were made from stock solutions immediately before experiments, and the stock solution of glutamate and FeCl₃ made fresh daily. 300 mM KCl, 300 mM NaCl, 300 mM MgCl₂, 2 μ M of the cell impermeant APG-4 TMA⁺ salt, or 10 μ M ThT were added where indicated.

Device loading and operation

24 hours before experiments, cells were streaked from -80°C glycerol stocks onto LB agar plates containing the selection antibiotics and grown overnight at 37°C. The day of experiments, single colonies from LB plates were inoculated into 1 mL of liquid MSgg medium, vortexed, and were immediately loaded into the growth chamber. Cells were immediately loaded into the growth chamber by filling the fluidic channel with the cell suspension and initiating a transient pressure spike in the device. This pressure spike temporarily increases the chamber depth and allows cell clusters to be trapped within the chamber. Additionally, the chamber pillars and walls are briefly lifted out of contact with the glass MEA substrate, trapping cells beneath these structures to serve as growth seeds. After loading, cells were grown in the MiCMA at 37°C for ~2 hrs before changing temperature to 30°C and growing overnight. Flow was controlled by a syringe pump (New Era Systems) and held at a constant rate of 50 μ L/hr.

About 1 hour prior to electrical stimulation, MSgg supplemented with 300 mM KCl was used to saturate the biofilm with potassium ions, since biofilms act as sinks for potassium. Flow was returned to standard MSgg (containing 8 mM KCl) 10-15 minutes prior to stimulation, and

standard MSgg media was used for the remainder of the experiment. This saturation step, while not strictly necessary to see the electrically induced proliferation of motile cells (Fig. S13), facilitated more consistent results. Individual electrodes were independently provided monophasic -3.0 V stimulation pulses with a pulse frequency of 50 Hz for 0.3 s (15 cycles of -3V followed by 0 V), unless noted otherwise, using the Multi Channel Experimenter software (Multi Channel Systems GmbH). Stimulation voltage was relative to the potential at the reference electrode. Stimulation parameters were selected based on previous literature (Stratford et al., 2019) and empirical testing. Specifically, the pulse amplitude was chosen to match the peak-topeak amplitude used by Stratford et al. (3Vpp AC 0.1 kHz for 2.5s). Following the recommendation of the MEA manufacturer, we only provided negative voltage rather than biphasic voltage stimulation, to avoid damage and electrolysis of the TiN electrodes. During initial testing of stimulation parameters, we imaged the membrane potential response to different voltage and frequency stimulations using Thioflavin-T (a Nernstian-potential fluorescent dye, ThT). Specifically, we applied an electrical stimulus to biofilms in the presence of 300 mM KCl. Under these conditions, cells around the electrode exhibit a more negative membrane potential after the stimulation (high ThT signal, Fig. S14A). The frequency and voltage of electrical stimulation were varied, and the probability of visualizing the ThT response was calculated. Fig. S14B shows an interpolated plot of the stimulation frequencies and voltages tested, showing that the highest probability of a cellular membrane potential response occurs with a stimulation of -3V and 50 Hz. In a separate experiment, media supplemented with 300 mM potassium ions elicits the greatest ThT response to -3V and 50 Hz stimulation, compared to 300 mM magnesium or sodium ion supplemented media (Fig. S14C).

Commercial microfluidics loading

24 hours prior to experiments, cells were streaked from -80°C glycerol stocks onto LB agar plates containing the selection antibiotics and grown overnight at 37°C. On the day of experiments, single colonies from LB plates were inoculated into 4 mL of liquid LB media and grown in a 37°C shaker for 3-4 hrs. Cultures were centrifuged at 4800 rpm for 2 min and resuspended in MSgg medium. Cells were immediately loaded beneath the support pillars (height 0.65 µm) in B04F microfluidic plates using the CellASIC ONIX microfluidic system (EMD Millipore). Cells were equilibrated on the plate at 37°C and ~16 mm s⁻¹ for 1 hour, before changing the temperature to 32.5°C. After 12-16 hours, the temperature was lowered to 30°C for the remainder of the experiment. Biofilms grew from beneath the support pillar, filling the 6 µm tall chamber. A repeated cycle of 40 minutes of MSgg supplemented with 300 mM KCl followed by 200 minutes of MSgg with a constant flow rate of ~32 μm s⁻¹ was used for repeated potassium shock experiments. 40 minutes of 300 mM KCl media was used to ensure enough time for the media to fully saturate the biofilm, as previous work suggests around 30 minutes are necessary (Yang et al., 2020). The 4-hour spacing between pulses was used to avoid the ~2.5-hour period of the innate potassium-mediated electrochemical signaling present in B. subtilis biofilms (Prindle et al., 2015). For the single shock experiments, a 40-minute shock was applied at 10 or 20 hours after changing the temperature to 30°C. A similar change in matrix and motile cell area was realized with a shock at either 10 or 20 hours.

Widefield microscopy

Phase-contrast and fluorescence microscopy images of biofilms were recorded at regular time intervals on both widefield and confocal microscopes. For widefield imaging of the electrical

device (Fig. 3), an Olympus IX83 inverted epifluorescence microscope with autofocus and a 10X, 0.3 NA objective were used. For each image, the minimum fluorescence exposure time that yielded good signal was used. For YFP images, the exposure time was 5 ms. For mCherry images, the exposure time was 50 ms.

Confocal microscopy

Confocal images of the commercial microfluidic device (Fig. 2), APG-4 around stimulated electrodes (Fig.1D), and z-stacks of the electrical device (Fig 4A, C, and E) were recorded with an Olympus FV3000 inverted confocal microscope with drift compensation. For the commercial microfluidic device, images were recorded using a 20X, 0.5 NA objective, just above the glass at the bottom of the chamber and showed that biofilms filled the height (z-dimension) of the growth chamber. The z-height of the chamber makes it possible for biofilms to have a depth of about 10 cell layers. For YFP images, a 514 nm, 40 mW laser with power reduced to 0.02% was used. For mCherry images, a 594 nm, 20 mW laser with power reduced to 0.8% was used. A scanning speed of 8 µs/pixel was used. For the APG-4 and z-stack imaging, images were recorded using a 40X, 1.25 NA silicone oil immersion objective. The APG-4 images were collected using the 8kHz resonant scanner, with YFP power reduced to 50%. Images of APG-4 within the biofilm were filtered with an 8-pixel median filter to suppress dead and compromised cells that strongly absorb APG-4. For the z-stacks of the electrical device, YFP power was reduced to 0.01%, mCherry power was reduced to 0.2%, and a sampling speed of 4 µs/pixel was used. Confocal time-lapse data (Fig. 4G and H) was recorded with a Nikon A1 R inverted, scanning confocal microscope with a 40X, 1.3 NA oil immersion objective. To prevent phototoxicity and bleaching during these experiments, the minimal laser power, pixel sampling time, and pixel density that enabled resolution of individual cells was used. For this reason, the intensity values for fluorescent reporters are different in the confocal time-lapse data and the z-stack data.

APG-4 radial profile and temporal analysis

For the radial profile plots of APG-4 (Fig.1E), the space around each electrode was divided into concentric circles with radii in increments of 500 nm, and the average pixel intensity was computed for all pixels in the rings. For the temporal analysis (Fig. S4B, C), the maximum intensity value of the radial profiles was plotted as a function of time. An exponential decay curve was fit to the 15 time points (7.5 seconds) following electrical stimulation, and the decay constant was used to estimate the duration of potassium accumulation around electrodes.

Pixel classification and cell-type ratio time-lapse analysis

To classify individual pixels from confocal images as mostly motile or matrix-producing (Fig. 2C, D, and F), contrast-limited adaptive histogram equalization was applied to each color channel individually to normalize the pixel intensities (*adapthisteq* function). Then the normalized intensities were compared to classify each pixel as either mostly matrix-producing, or mostly motile. The image region considered for analysis consisted of approximately half of the biofilm, excluding the area under the support pillar. For widefield microscopy images (Fig. 3C and D), the ratio of the YFP to mCherry fluorescence signals was considered. A threshold at timepoint 0 hours was manually determined for each electrode. The region within 40 μm of the electrode edge was considered. For both confocal and widefield images, the area percent was calculated from the pixel classification maps as the area of the given cell type (matrix-producing

or motile), divided by the total area. All pixel classification analysis was performed in MATLAB.

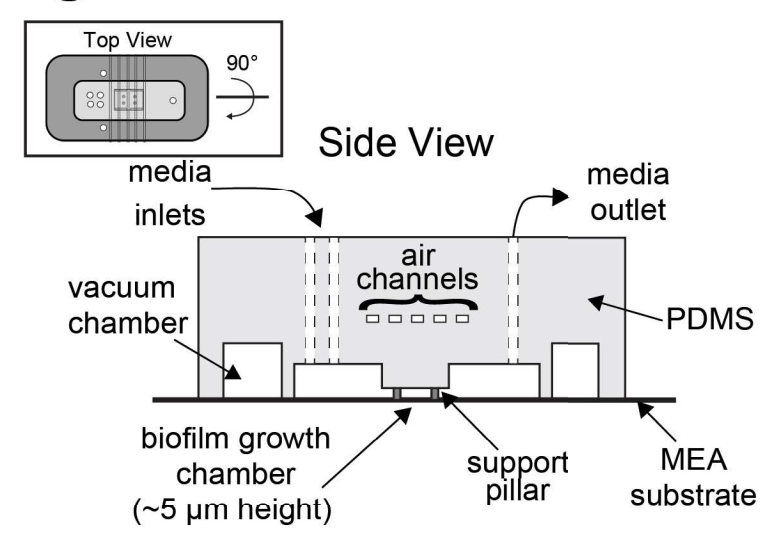
Confocal cell analysis

To analyze confocal stacks, individual cells were segmented in the z-plane directly above the electrode array using the Trainable Weka Segmentation plugin in Fiji (Arganda-Carreras et al., 2017). Within each segmented cell, the mean intensity value for *Phag*-YFP and *PtasA*-mCherry were calculated. Throughout the paper, the natural logarithm of those values, the ratio of those values, or the natural logarithm of the ratio is used. The cells exhibited a bimodal distribution of log(*Phag*-YFP) values, allowing the use of a threshold at the minimum between the two modes to distinguish *hag* cells (Fig. S10). For the analysis of cell-type distributions around stimulated electrodes (Fig. S9B), regions of high ThT (directly around stimulated electrodes) and low ThT (away from the electrode) were manually identified. In the curves of Fig. 4B and D, the space around electrodes was divided into concentric circles with radii in increments of 7 μm, and the fraction of *hag* cells with centroids between each set of concentric radii was computed. To produce the distributions of Fig. S10, 2-D histograms were created of single-cell log(*Phag*-YFP) and log(*PtasA*-mCherry) values for every cell with its centroid within 5 μm of the electrode, and contour maps were created from those 2-D histograms.

To extract time traces and lineage information from confocal time-lapse data (Fig. 4G and H), we manually tracked cell lineages with the mTrackJ plugin in Fiji (Meijering et al., 2012), determining the point of division when daughter cells clearly separated in fluorescence movies. All single-cell data analysis was performed in Python.

Supplemental References

- Arganda-Carreras, I., Kaynig, V., Rueden, C., Eliceiri, K.W., Schindelin, J., Cardona, A., and Seung, H.S. (2017). Trainable Weka Segmentation: a machine learning tool for microscopy pixel classification. Bioinformatics *33*, 2424–2426.
- Irnov, I., and Winkler, W.C. (2010). A regulatory RNA required for antitermination of biofilm and capsular polysaccharide operons in Bacillales. Molecular Microbiology *76*, 559–575.
- Meijering, E., Dzyubachyk, O., Smal, I., and conn, P.M. (2012). Chapter nine Methods for Cell and Particle Tracking. (Academic Press), pp. 183–200.
- Prindle, A., Liu, J., Asally, M., Ly, S., Garcia-Ojalvo, J., and Süel, G.M. (2015). Ion channels enable electrical communication in bacterial communities. Nature *527*, 59–63.
- Stratford, J.P., Edwards, C.L.A., Ghanshyam, M.J., Malyshev, D., Delise, M.A., Hayashi, Y., and Asally, M. (2019). Electrically induced bacterial membrane-potential dynamics correspond to cellular proliferation capacity. Proc National Acad Sci *116*, 9552--9557.
- VanDelinder, V., and Groisman, A. (2007). Perfusion in Microfluidic Cross-Flow: Separation of White Blood Cells from Whole Blood and Exchange of Medium in a Continuous Flow. Anal Chem 79, 2023–2030.
- Yang, C.-Y., Bialecka-Fornal, M., Weatherwax, C., Larkin, J.W., Prindle, A., Liu, J., Garcia-Ojalvo, J., and Süel, G.M. (2020). Encoding Membrane-Potential-Based Memory within a Microbial Community. Cell Syst *10*, 417-423.e3.



Microfluidic Component

Fig. S1. Schematic sideview of the two-layer PDMS microfluidic device. Engraved on the bottom surface of the PDMS chip is an O-shaped vacuum chamber groove to seal the chip to the MEA substrate. A perfusion flow channel, with one or more media inlets and a media outlet, supplies fresh media to the 2 mm x 2 mm square biofilm growth chamber. When under vacuum, the biofilm growth chamber has a height of \sim 5 μ m that is maintained by the support pillars. Embedded in the chip are air channels, which expose the top of the 100 μ m-thick PDMS roof of the growth chamber to atmospheric air, facilitating aerobic growth of bacteria in the chamber. (Not to scale)

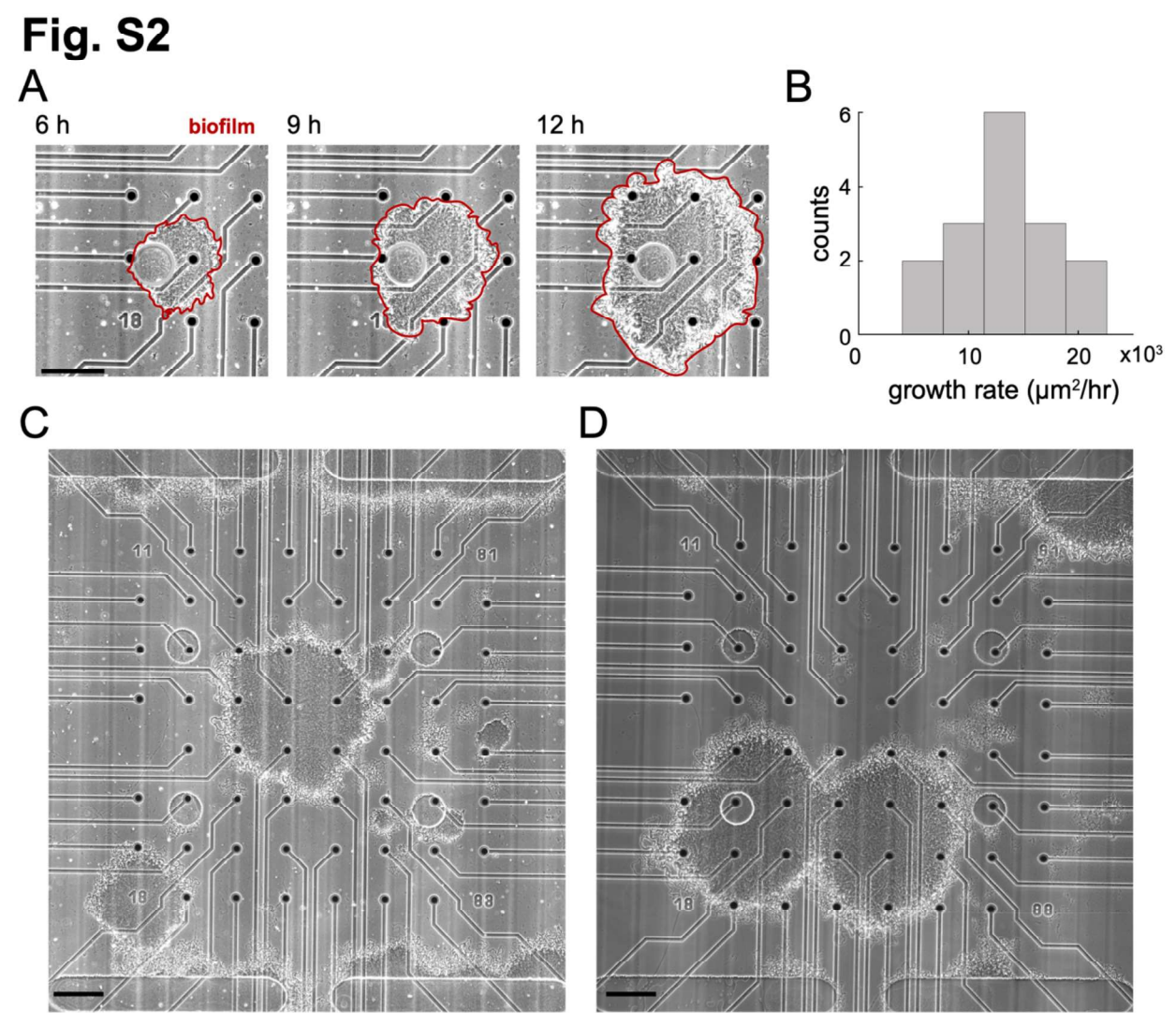


Fig. S2. Biofilm growth in the device. (A) A filmstrip of phase-contrast images shows a biofilm growing over an electrode array in the MiCMA. Timestamps indicate hours since cell loading. Red lines show the biofilm border (scale bar 200 μ m). (B) A histogram of measured biofilm expansion rates with a mean expansion rate of 14,460 \pm 1,880 μ m²/hr (mean \pm SEM, N = 16 biofilms) during the first 12 hours of growth in the device. Expansion rate is calculated as the mean rate of increase in biofilm area over time. (C, D) Phase-contrast images showing the entire MiCMA growth chamber with several biofilms growing at random locations within the chamber (scale bars 200 μ m).

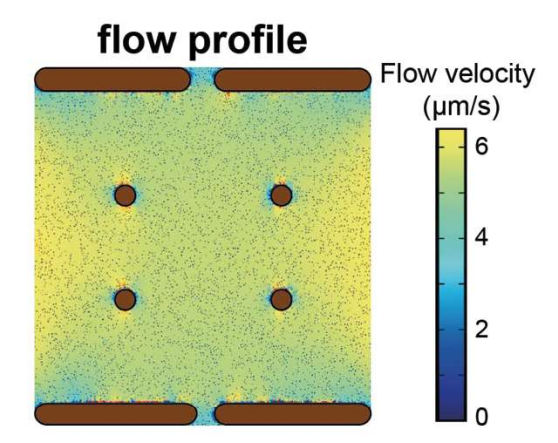


Fig. S3. Media flow in the growth chamber. Color-coded map of the flow velocity in the midplane of the growth chamber from numerical simulations performed for the experimentally measured total volumetric flow rate of 50 μ L/hr through the microfluidic device and velocity of 5.5 μ m/sec in the growth chamber.

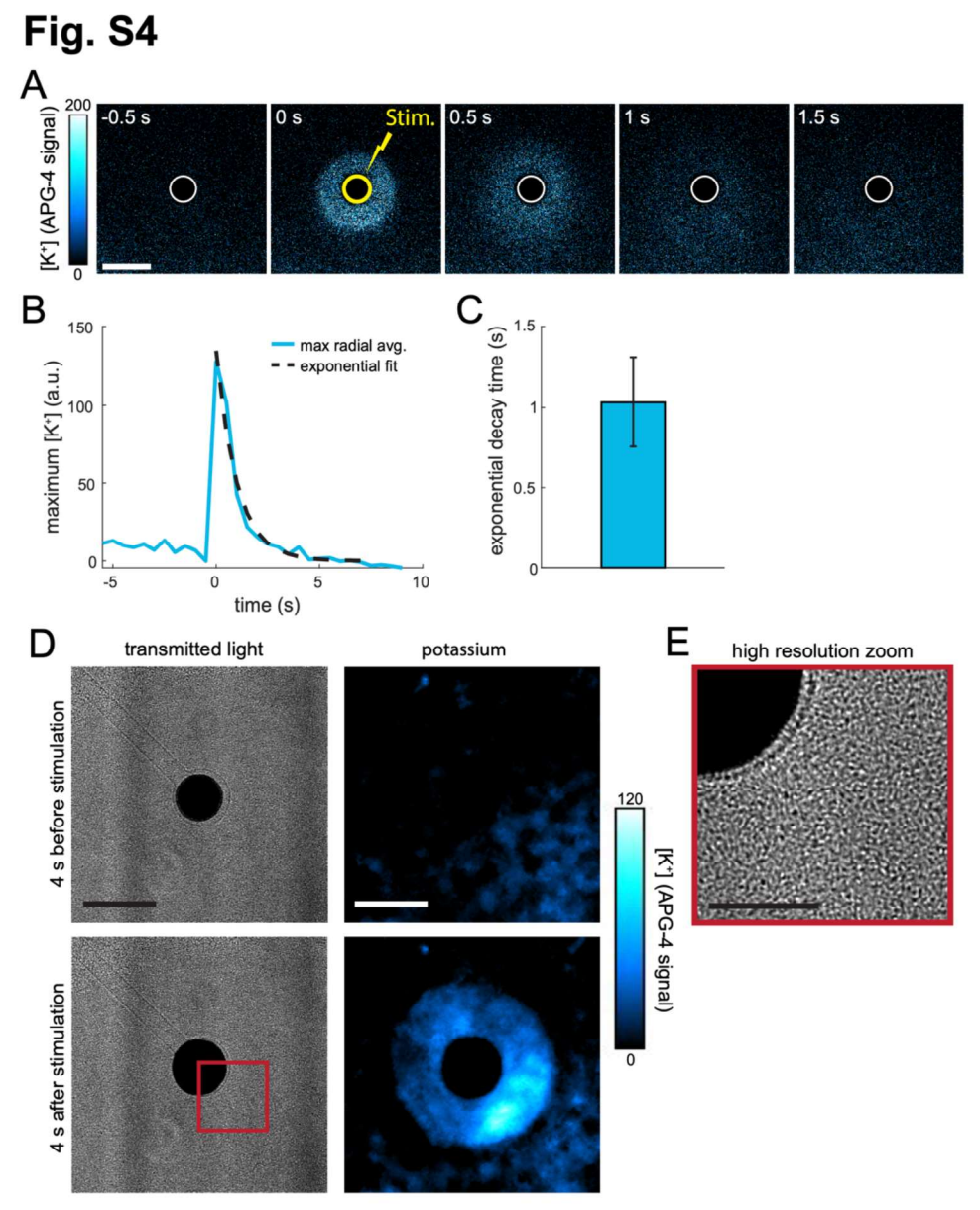


Fig. S4. Characterization of potassium ion concentration around stimulated electrodes. (A) Filmstrip of the potassium sensitive fluorescent dye APG-4 near an additional electrode (gray circle) before and after stimulation (stimulation shown in yellow, at 0 seconds). The fluorescence intensity (in blue-white) indicates the potassium concentration (scale bar 50 μm). (B) The maximum radial average potassium concentration (within 100 μm of the electrode) as a function of time is shown in blue for the electrode shown in (A). The black dashed line shows an exponential fit used to calculate the decay time. (C) The average decay time for the potassium enrichment around stimulated electrodes is 1.03 ± 0.28 seconds (mean ± SEM, N = 6 stimulations). (D) Transmitted light (left column) and fluorescent images of APG-4 (right column) around an electrode embedded within a biofilm 4 seconds before (top row) and 4 seconds after (bottom row) electrical stimulation. Fluorescence images have been spatially median filtered to diminish the signal from dead cells, which absorb APG-4 (scale bars 50 μm). (E) A high resolution transmitted light image of the region denoted by the red box in (D) (scale bar 20 μm).

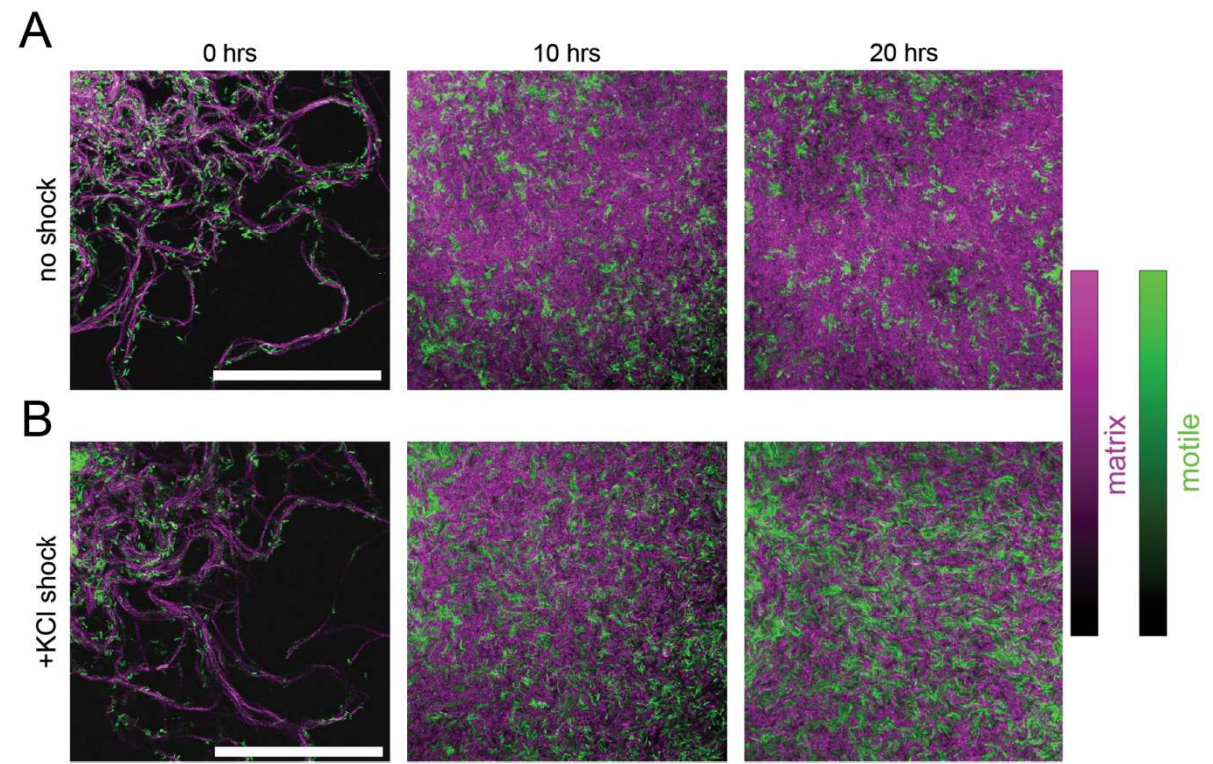


Fig. S5. Fluorescence images of cell-type during transient enrichment of potassium in the growth media. (A) Filmstrip of a biofilm growing in standard MSgg media, showing the fluorescence images corresponding to the cell-type pixel maps in Fig. 2D. (B) Filmstrip of a biofilm that is transiently shocked with growth media supplemented with 300 mM potassium every 4 hours for 40 minutes, showing the fluorescence images corresponding to the cell-type pixel maps in Fig. 2F. The color contrast is set individually for each timepoint (Scale bars 100 μm).

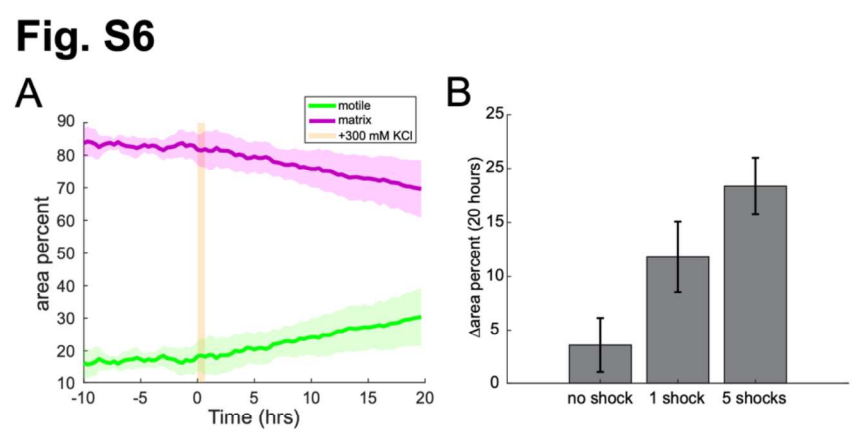


Fig. S6. A single enrichment of potassium in the growth media increases the percentage of motile cells within the biofilm. (A) Plot of the average motile and matrix area percent for biofilms subject to a single, 40-minute pulse with growth media supplemented with 300 mM potassium. (B) Plot of the change in motile area percent over 20 hours. Biofilms are provided either conventional growth media (no shock, data from Fig. 2E), a single shock (1 shock, data from Fig. S6A), or periodic shock with media supplemented with 300 mM KCl (5 shocks, data from Fig. 2G). Error bars show the mean \pm SEM, from N = 8 biofilms for no shock and 5 shocks, and N = 4 biofilms for 1 shock.



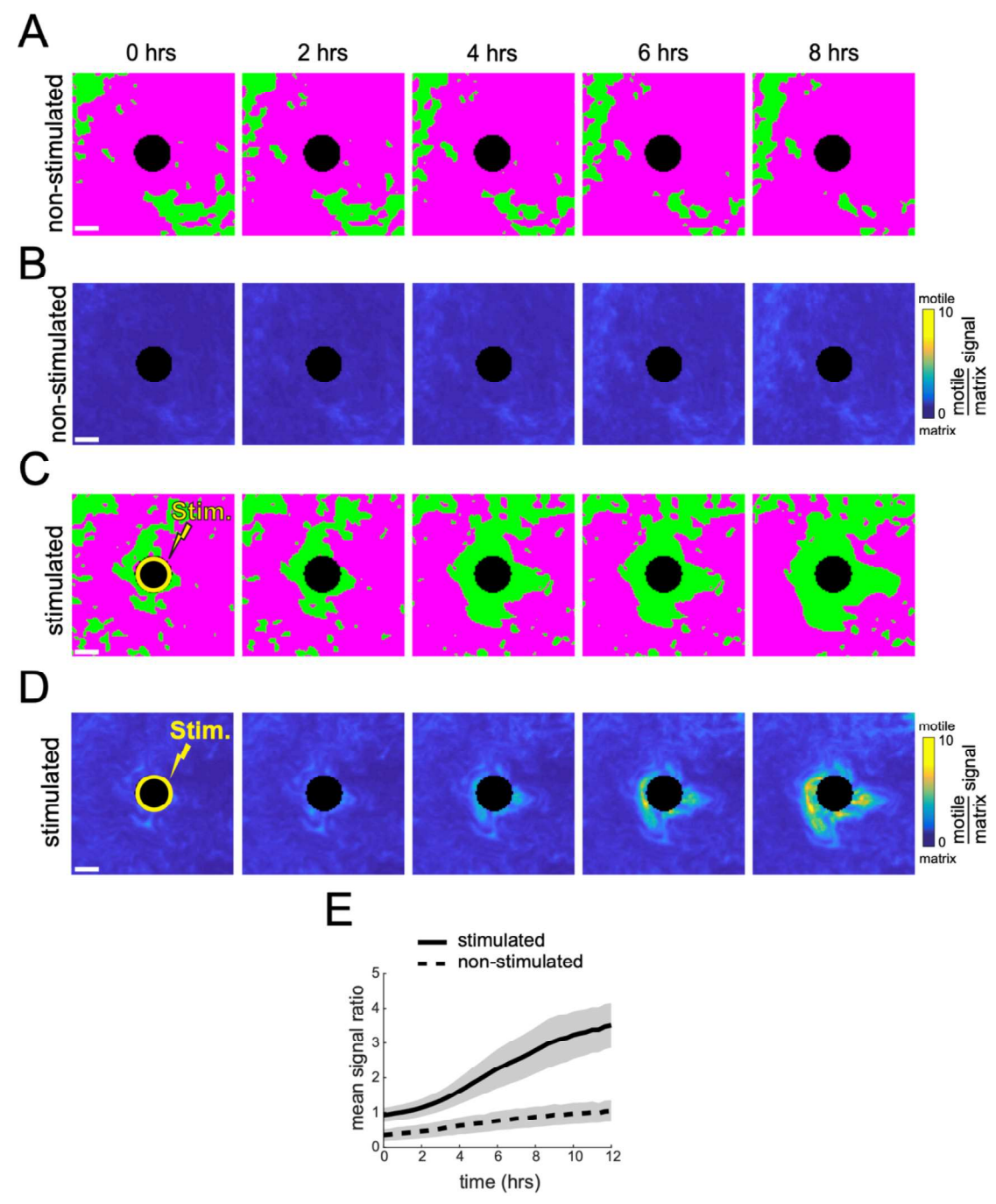


Fig. S7. Cell-type pixel maps and signal ratios around electrodes. (A, B) Filmstrips of the (A) cell-type pixel maps (motile in green and matrix in magenta) and (B) signal ratio around the non-stimulated electrode from Fig. 3C. (C, D) Filmstrips of the (C) cell-type pixel maps and (D) signal ratio around the stimulated electrode from Fig. 3D. (Scale bars 20 μ m). (E) The mean signal ratio (within 5 μ m of the electrode) as a function of time for stimulated (solid line) and non-stimulated (dashed line) electrodes. Error bars show the mean \pm SEM, from N = 8 stimulated electrodes and N = 4 non-stimulated electrodes.

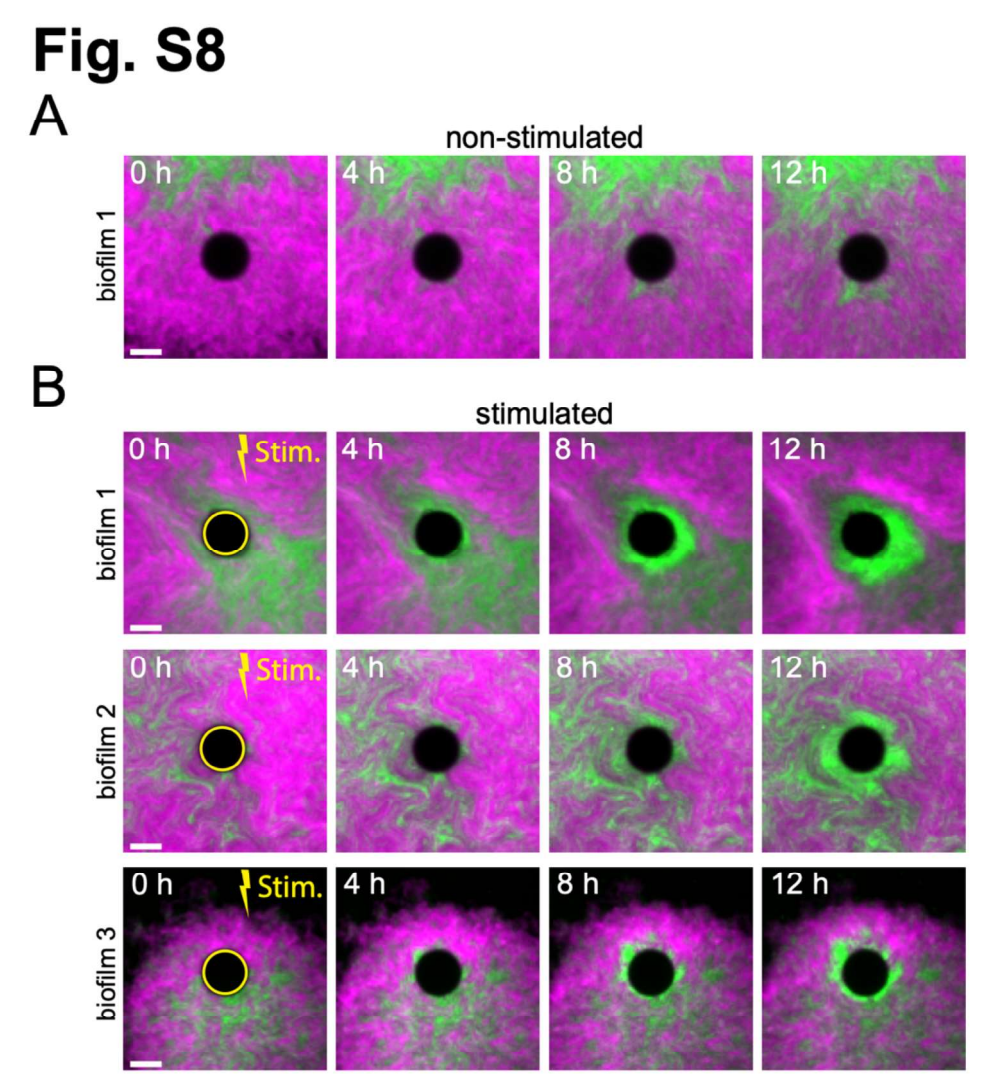


Fig. S8. Fluorescence time lapse images around electrodes. (A) Filmstrip of fluorescence microscopy images around an additional unstimulated electrode. **(B)** Similar filmstrips around three additional stimulated electrodes from 3 different biofilms (motile in green and matrix in magenta, Scale bars 20 μm).

Fig. S9 A motile/matrix ThT B cell type distributions motile motile matrix figure 12 hr low ThT regions regions

Fig. S9. Enhanced motile region around stimulated electrodes exhibits high ThT signal. (A) Confocal fluorescence images showing motile and matrix-producing cells (left) and ThT (right) 12 hours after stimulating the electrode (scale bar $10 \mu m$). (B) Pie charts showing the percentage of motile and matrix cells in low ThT regions (left, away from the electrode) and high ThT regions (right, surrounding the electrode). Labels indicate the mean percentage \pm SEM from N = 4 electrodes.

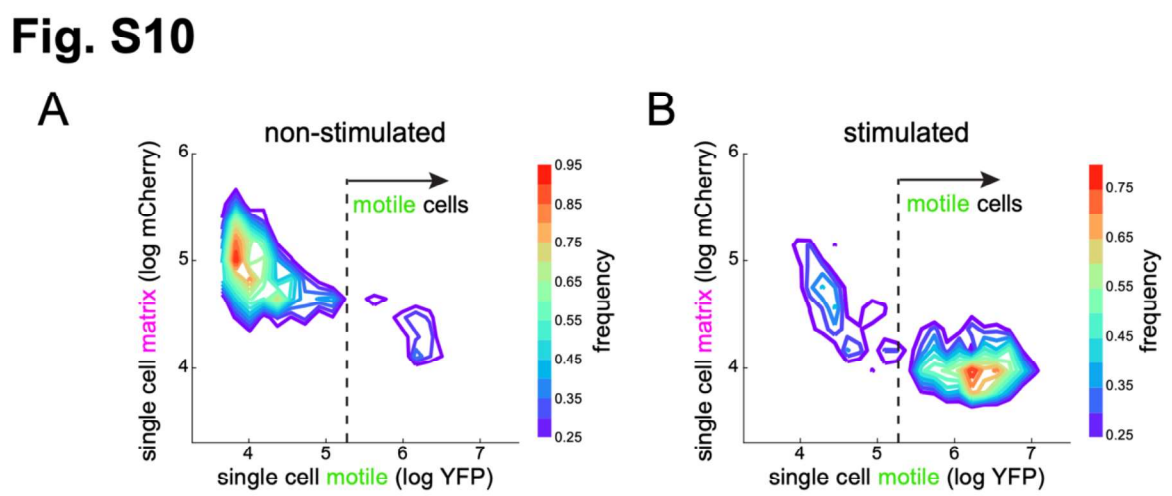


Fig. S10. Electrical stimulation causes a local increase in motile cells. (A) Single-cell gene contour plot for all cells within 5 μm of unstimulated electrodes. The color bar (right) illustrates the relative frequency of expression. **(B)** Single-cell gene expression contour plot for all cells within 5 μm of stimulated electrodes. Motile cells are identified by thresholding the YFP fluorescence signal at the vertical dashed line. For unstimulated electrodes, a majority of cells (69%) are matrix-producing, while for stimulated electrodes a majority of cells (53%) are motile.

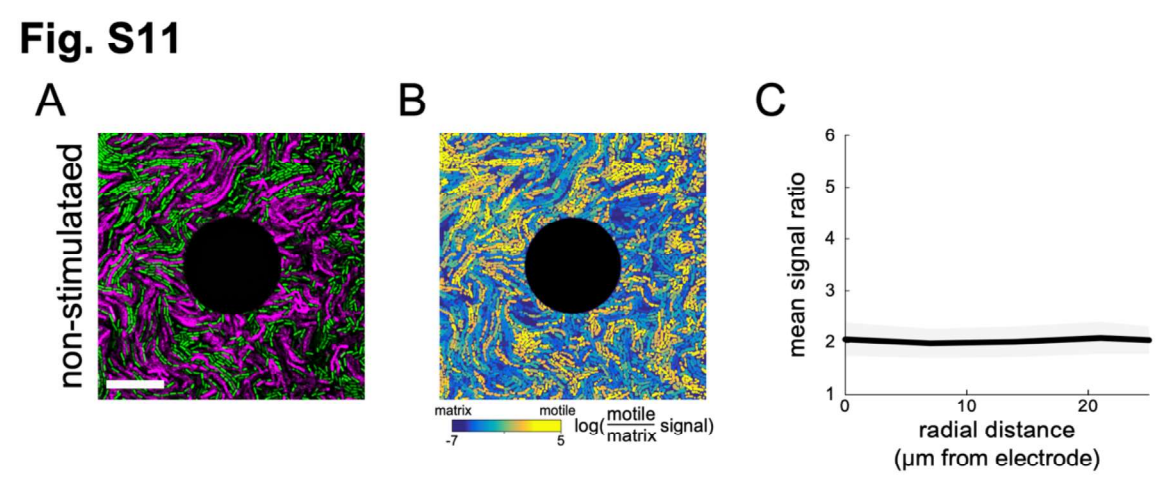


Fig. S11. Single cell distribution and expression ratio. (A) Confocal fluorescence images showing motile and matrix-producing cells surrounding a non-stimulated electrode (scale bar 20 μ m). (B) Segmented confocal image for the same non-stimulated electrode where each cell has been colored according to the ratio of P_{hag}/P_{tasA} . (C) Radial plot of the average single-cell P_{hag}/P_{tasA} ratio near a non-stimulated electrode shows no radial dependence.

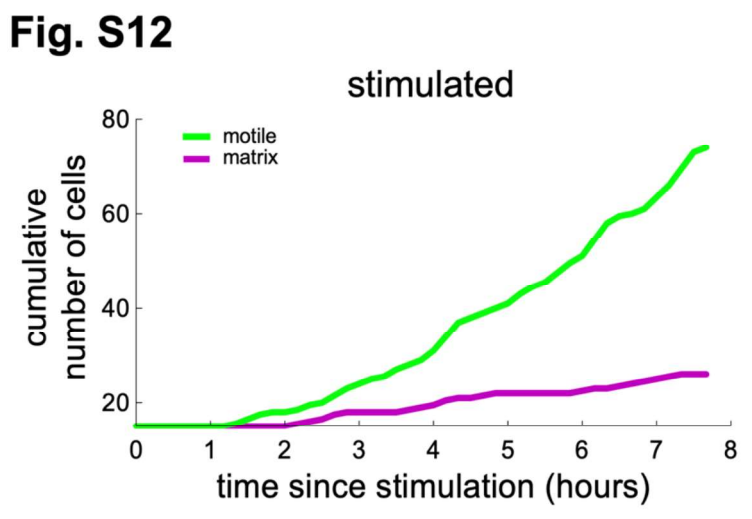


Fig. S12. Enhanced proliferation of motile cells around stimulated electrodes. Cumulative cell total, starting from 15 of each cell-type, as a function of time.

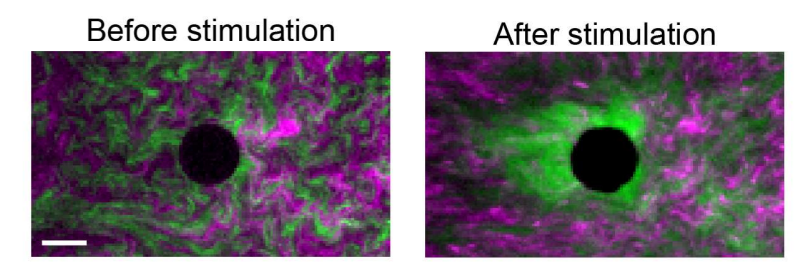


Fig. S13. Response in electrodes not pre-saturated with 300 mM KCl. Fluorescence microscopy images of cell type before (left) and after (right) electrical stimulation (Scale bars 20 μ m).